Crustal deformation and fault slip during the seismic cycle in the North Chile subduction zone, from GPS and InSAR observations

M. Chlieh,[1,][*] J. B. de Chabalier,[1] J. C. Ruegg,[1] R. Armijo,[1] R. Dmowska,[2] J. Campos[3] and K. L. Feigl[4]

[1]*Institut de Physique du Globe de Paris, Départements de Tectonique et de Sismologie, CNRS UMR 7578 & 7580, 4 Place Jussieu, 75252 Paris cedex* 05, *France. E-mail: chlieh@ipgp.jussieu.fr*
[2]*Division of Engineering and Applied Sciences, Harvard University, Cambridge,* MA 02138, *USA*
[3]*Departamento de Geofísica de la Universidad de Chile, Santiago, Chile*
[4]*CNRS, Toulouse, France*

SUMMARY
The different phases of the earthquake cycle can produce measurable deformation of the Earth's surface. This work is aimed at describing the evolution of that deformation in space and time, as well as the distribution of causal slip on the fault at depth. We have applied GPS and synthetic aperture radar (SAR) interferometry (InSAR) techniques to northern Chile, where fast plate convergence rates are associated with large subduction earthquakes and extensive crustal deformation. The region of northern Chile between 18°S and 23°S is one of the most important seismic gaps in the world, with no rupture having occurred since 1877. In 1995, the $M_w = 8.1$ Antofagasta earthquake ruptured the subduction interface over a length of 180 km in the region immediately to the south of this 450 km long gap. The coseismic deformation associated with this event has been documented previously. Here we use GPS position time-series for 40 benchmarks (measured between 1996 and 2000) and ERS SAR interferograms (for the interval between 1995 and 1999) to map both the post-seismic deformation following the 1995 event and the ongoing interseismic deformation in the adjacent gap region. In the seismic gap, the interseismic velocities of 20–30 mm yr^{-1} to the east with respect to South America are mapped. Both the GPS and the InSAR measurements can be modelled with 100 per cent coupling of the thrust interface of the subduction to a depth of 35 km, with a transition zone extending down to 55 km depth. The slip rate in that zone increases linearly from zero to the plate convergence rate. South of the gap, the interferometric map shows interseismic deformation superimposed with deformation following the 1995 earthquake and covering the same area as the coseismic deformation. Some 40 per cent of this deformation is related to seismic activity in the 3.3 yr following the 1995 event, in particular slip during a $M_w = 7.1$ earthquake in 1998. However, most of the signal (60 per cent) corresponds to post-seismic deformation resulting from widespread aseismic slip in the subduction interface. The afterslip appears to have occurred down-dip in the transition zone at 35–55 km depth and to have propagated laterally northwards at 25–45 km depth under the Mejillones Peninsula, which is a prominent geomorphological feature at the boundary between the 1877 and 1995 rupture zones. We propose a simple slip model for the seismic cycle associated with the Antofagasta earthquake, where the transition zone alternates between aseismic shear and seismic slip.

Key words: earthquake cycle, GPS, InSAR, northern Chile, subduction zone.

1 INTRODUCTION

The goal of this paper is to provide insight into the mechanics of a subduction interplate contact and the surface deformation associated with its seismic cycle. The characteristics of strain accumulation and release down-dip of the seismogenic contact are still not well defined or understood. While the observed coseismic surface deformation can be adequately explained by slip on a fault modelled using elastic dislocations, opinion is divided on the importance of aseismic slip, post-seismic transients and interseismic strain accumulation. Of particular importance is the behaviour of the

*Now at: California Institute of Technology, Pasadena, US. E-mail: chlieh@gps.caltech.edu

transition zone separating regions of the fault dominated by stable sliding and stick-slip.

Geodetic measurements document subtle crustal deformation events at strain rates below that detectable by most forms of seismic instruments. Although the development of GPS and synthetic aperture radar (SAR) interferometry (InSAR) in the last decade has allowed geophysicists to start exploring these topics (Thatcher 1984; Dragert et al. 1994; Cohen & Freymueller 1997; Peltzer et al. 2001), fundamental questions remain open. How does surface deformation evolve in space and time over an underthrusting fault as it experiences an earthquake rupture (instantaneous coseismic deformation), a subsequent relaxation (post-seismic deformation over days to decades) and a further loading (interseismic deformation over decades to centuries)? What is the relation between stick-slip (seismic, brittle rupture) and stable sliding (aseismic, plastic creep) in different regions of the fault? Do the mechanics and kinematics of slip vary in space and time along both strike and dip? Answering these questions is fundamental to understanding rupture and earthquake mechanics, and necessary to estimate seismic hazard in a given area.

We address these questions by analysing the time–space evolution of the surface deformation related to slip on a great underthrust during a meaningful portion of its seismic cycle. We focus on a section of the North Chile subduction zone and analyse surface deformation fields using a combination of InSAR, GPS and seismological data. There are many reasons why this region is particularly interesting: First, convergence between the Nazca and South America plates occurs at a fast rate (about 8 cm yr^{-1}) producing large ($M > 8$) subduction earthquakes which ensure surface displacement fields that are easily observable in broad land areas alongside the trench. In addition, the atmospheric conditions of the Atacama Desert in northern Chile are favourable for obtaining SAR interferograms with excellent correlation over long time periods. Second, northernmost Chile is currently a seismic gap; the area has been quiescent for 125 yr after the occurrence of a $M > 8$ earthquake in 1877. However, in 1995 July the $M_w = 8.1$ Antofagasta earthquake ruptured a 180 km-long segment just south of the main 1877 gap. The region thus offers an opportunity to measure and analyse the evolution of surface deformation related to the 1995 earthquake rupture, transient post-seismic relaxation and the interseismic loading processes.

We investigate post-seismic slip in the 3.3 yr following the 1995 Antofagasta earthquake, as well as the current interseismic deformation in the seismic gap, north of the 1995 rupture (Fig. 1). The Antofagasta earthquake rupture is separated from the southern end of the 1877 gap by the Mejillones Peninsula region, which is a major geomorphological feature along the subduction zone (Armijo & Thiele 1990). The combination of descending tracks of ERS-1 and 2 radar images with east–west GPS profiles records the deformation, in directions both parallel and perpendicular to the tectonic structure of the Andes, allowing us to reconstruct most of the earthquake cycle.

2 SEISMOTECTONICS OF SOUTHERN PERU/NORTHERN CHILE

2.1 Seismic gap and depth extent of the seismogenic zone

The most recent large subduction earthquakes ($M_w > 7.7$) along the Peru–Chile trench are shown in Fig. 1, with the area of our research marked as a dashed-line rectangle around the Arica corner. Here the Nazca Plate subducts under South America with conver-

gence rate estimates between 64 and 79 mm yr^{-1} (DeMets et al. 1994; Angermann et al. 1999). The corner is characterized by two famous seismic gaps that mark the zones of the 1868 August 14 ($M_t = 9.0$) southern Peru and the 1877 May 9 ($M_t = 9.0$) northern Chile earthquakes. The southern Peru 1868 rupture segment broke previously in 1604 and 1784 in a similar, approximately 450 km long rupture. The northwest part of that segment broke again in a $M_w = 8.4$ earthquake on 2001 June 23, filling at least partially the South Peru gap (Ruegg et al. 2001).

The North Chile segment of the gap is approximately 450 km long. Currently in the interseismic interval (Bevis et al. 2001; Klotz et al. 2001), it last ruptured in the great 1877 earthquake which produced damage along the coast of northern Chile and destructive tsunamis. There is no information about earlier great earthquakes in this region. The zone is well known as a seismic gap (Kelleher 1972; Nishenko 1985), with recurrence time estimates ranging from 111 to 264 yr (Comte & Pardo 1991; Nishenko 1991).

The depth extent of the seismically coupled interface in the area of the Antofagasta rupture and the segment north of it has been investigated by many researchers. Tichelaar & Ruff (1991, 1993) concluded that the lower seismogenic depth for that area was at 36–41 km, based on the presence of thrust interplate events of magnitude 6 or larger. A study of seismicity along the interplate interface (thrust) and in the slab (normal) led Comte & Suárez (1995) to the conclusion that the lower end of the coupled zone is at 60 ± 10 km depth, while Delouis et al. (1997) placed it at 50 km. Accurate locations for the aftershocks of the 1995 Antofagasta event placed the down-dip limit at 46 km depth (Husen et al. 1999).

2.2 The Antofagasta earthquake

The 1995 July 30 ($M_w = 8.1$) Antofagasta earthquake started under the southern part of the Mejillones Peninsula, at a depth of 36 km (from local network data; Delouis et al. 1997); the NEIC gave a hypocentral depth of 47 km, and 41 km depth was found from global teleseismic earth-quake relocation (Engdahl et al. 1998). It ruptured 180 km to the south, with a smooth, slightly heterogeneous slip distribution. The rupture process has been extensively studied using seismological and geodetic techniques. Combined with GPS, InSAR (Fig. 2) has proven to be necessary to constrain the surface deformation and to characterize the mechanics and kinematics of the earthquake. InSAR and GPS measurements (Ruegg et al. 1996; de Chabalier et al. 1997; Klotz et al. 1999; Pritchard et al. 2002) show that the area of coseismic deformation is very large (200 × 300 km) reaching 60 cm of range increase and 1 m of horizontal displacement in Antofagasta city (Fig. 2). The horizontal coseismic displacement direction is parallel to the Nazca–South America relative plate convergence, indicating no slip partitioning (Ruegg et al. 1996; Klotz et al. 1999). The coseismic slip concentrates in a depth interval of 10–50 km, with very little slip below 40 km (Ruegg et al. 1996; Delouis et al. 1997; Ihmlé & Ruegg 1997; de Chabalier et al. 1998). All the seismic, geodetic or seismic/geodetic slip inversions give a consistent picture of the slip distribution during the earthquake with a single asperity slipping 5 to 10 m (Ruegg et al. 1996; Delouis et al. 1997; Carlo et al. 1999; Pritchard et al. 2002, and this study).

2.3 Seismicity after the Antofagasta earthquake

Two observations indicate that the Mejillones Peninsula acted as a barrier for the 1995 Antofagasta rupture: The aftershocks in the first 20 hr are confined to the area south of the
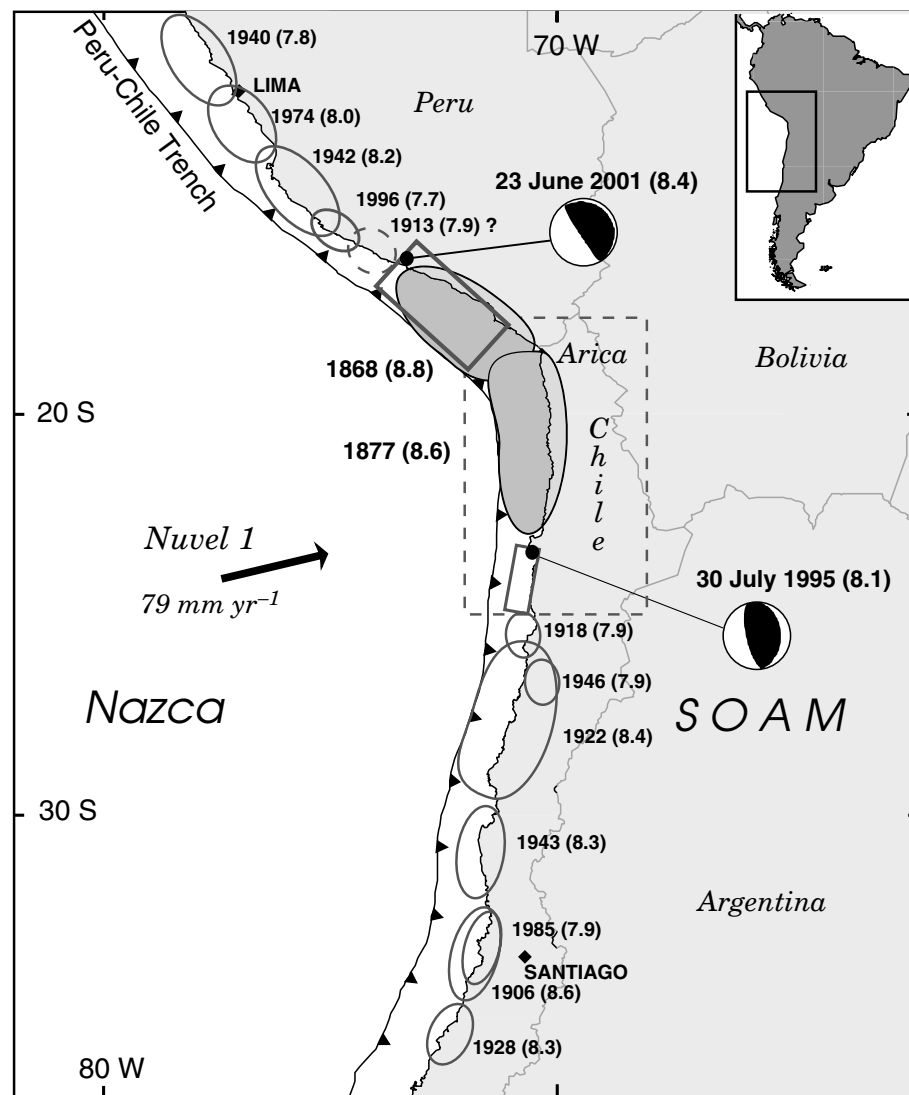
Figure 1. Large subduction earthquakes ($M_w > 7.7$) along the Peru–Chile trench. Grey ellipses represent the approximate extent of rupture zones. The study area (dashed rectangle) is located in the region of the Arica corner which ruptured in two 450 km long subduction earthquakes (hatched areas) in 1868 (South Peru) and in 1877 (North Chile). On 2001 June 23 southern Peru was affected by a strong $M_w = 8.4$ earthquake (rectangle from Ruegg *et al.* 2001), almost coinciding with the northern part of the 1868 rupture area. In northern Chile, no great event had been recorded since 1877. The $M_w = 8.1$ Antofagasta earthquake of 1995 July 30 ruptured a 180 km long segment (rectangle from Ruegg *et al.* 1996) located south of the 1877 rupture zone. The direction of plate motion in the area of the Arica corner is from Nuvel-1A.

Peninsula, while in the next 2 weeks and later the aftershocks also moved north (Delouis *et al.* 1997). Also, the spatial distribution of hypocentres of over 1200 aftershocks of the 1995 Antofagasta main shock and the *b* value (0.5) minimum coincide with the peninsula. This observation can be interpreted as indicating higher stress there (see also e.g. Wiemer & Wyss 2002). It is thought that that peninsula area acted as a barrier for the 1877 earthquake, just as it also acted as a barrier for the 1995 Antofagasta rupture.

In the period of observation covered by the InSAR data (described below), five earthquakes with $M_w \geq 6.0$ occurred in the area of Antofagasta. The largest and the deepest one was $M_w = 7.1$ on 1998 January 30 at approximately 23.9°S. It initiated deeper than the coseismic rupture of the 1995 earthquake, according to the USGS catalogue, although from global teleseismic earthquake relocation (Engdahl *et al.* 1998) it is located at 41 km depth, similar to the Antofagasta hypocentre. Although classical body-wave pro-

cedures do not determine the location of this aftershock very well, InSAR can place tighter constraints on its source parameters, as we shall describe below. Moreover InSAR can measure aseismic slip in addition to seismic slip to recover the total slip.

3 DATA ACQUISITION

3.1 InSAR measurements

We use the ERS-1 and ERS-2 radar images from the satellite descending track number 96 to produce two interferograms with temporal separations of 3.3 yr (Pair 1, Fig. 3a) and 3.6 yr (Pair 2, Fig. 3b), after the 1995 July 30 Antofagasta earthquake. Pair 1 starts 6 hr after the earthquake and therefore includes most of the post-seismic deformation. Pair 2 starts 70 days after the earthquake. The Pair 1 interferogram coincides with the three southern frames of Pair 2,

Table 1. SAR data used to compute Pair 1 and Pair 2 interferograms described in Fig. 3. Satellite ERS-1 and ERS-2 are denoted (E1) and (E2).

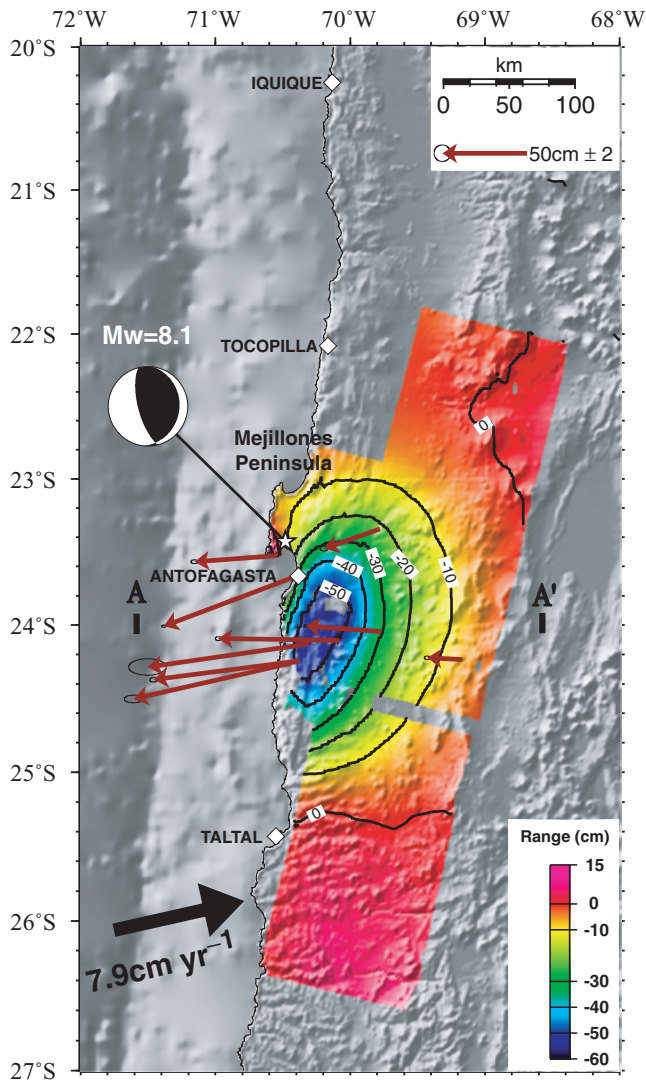| ERS Track/Frame	Date	Descending orbit 1/2	Ha[a](Frame 4077)
Pair 1: 96/4059-4095	1995 July 30/1998 November 2	21126(E1)/18487(E2)	−743
Pair 2: 96/3987-4095	1995 October 8/1999 May 31	22128(E1)/21493(E2)	−810
Tandem: 96/4059-4113	1996 March 31/1996 April 1	24635(E1)/4960(E2)	87

[a]Ambiguity height

Figure 2. Unwrapped coseismic interferogram and GPS measurements of the 1995 July 30 Antofagasta earthquake (de Chabalier *et al.* 1997). This interferogram is composed from images taken on three descending satellite tracks, 96, 325 and 368. It is presented unwrapped with contour lines every 10 cm. The white star shows the location of the main shock, and the Harvard Centroid Moment Tensor (CMT) solution for the earthquake is shown. The GPS vectors are presented in Table 2, and plotted relative to stable South America.

which covers seven frames corresponding to a total area of 700×100 km^2 along the coast of northern Chile.

We process the SAR data using the CNES/PRISME/DIAPASON software suite provided by Delft University (Scharroo & Visser 1998). The interferograms produce measurements of surface displacement in the satellite line of sight, but also contain effects of the difference in the orbital geometry, topography and atmospheric changes. To remove the topographic signal we combine the two-pass

method (Massonnet *et al.* 1993) and four-pass method (Gabriel *et al.* 1989). The preliminary orbital information comes from trajectories estimated within 20 cm by Delft University (Scharoo & Visser 1998).First, large topographic wavelengths are removed with the pre-existing crude GTOPO30 digital elevation model (DEM). The short-wavelength topographic residues are then removed by subtracting an interferogram spanning 1 day (tandem pair). The pulse repetition frequency (PRF) varies between acquisition of the two images of the Pair 1 interferogram. This creates a ramp of dense parallel fringes perpendicular to the azimuth. We corrected it by subtracting a simulated opposite ramp.

The interferograms are filtered using a weighted power spectrum algorithm (Goldstein & Werner 1998) and automatically unwrapped (Fig. 4) following Goldstein *et al.* (1988). The aridity of the Atacama Desert and the high altitude of ambiguity (more than 700 m) provide us with interferograms (Fig. 3) with an exceptionally high correlation. The small undulations in the fringes probably indicate atmospheric contaminations that are unrelated to the deformation.

These interferograms represent the scalar displacement along the line of sight direction with a mean unit vector with east, north and up components corresponding to 0.37, −0.09 and 0.91 respectively that we assume constant across the interferogram. Therefore, they represent mostly vertical, with some horizontal (mainly east–west) displacement (Fig. 3). Both interferograms exhibit two different patterns separated by the Mejillones Peninsula. North of the Peninsula, the fringes are elongated parallel to the trench, and correspond to about two fringes of relative range decrease (Fig. 3). The pattern is identical in both interferograms and extends beyond the edge of the image. We interpret this signal to be purely interseismic loading, consistent with the eastward displacements determined by GPS, as we show later.

South of the Mejillones Peninsula, the signal shows a large deformed region that encompasses the whole region of coseismic deformation (compare with Fig. 2). In the line of sight of the ERS radar, it is composed of an uplift (decreasing range) flanked far inland by a subsidence (increasing range). We interpret this signal as postseismic deformation with the possible superposition of interseismic deformation. The difference between Pair 1 and Pair 2 interferograms mostly concerns the background signal in the southern area and is difficult to interpret. To ensure the most complete picture of the post-seismic deformation in the southern area, including the 70 days following the main shock, we have created a composite interferogram (Fig. 4), replacing the southern part of the Pair 2 interferogram with the Pair 1 interferogram. The Pair 2 interferogram has been scaled to the same time interval as the Pair 1 interferogram, assuming a constant interseismic rate of range change.

3.2 GPS measurements and results

The GPS measurements included in this study resulted from a French–Chilean project (Ruegg *et al.* 1996) initiated in 1991 with the aim of a better understanding of the mechanics and kinematics of processes associated with the earthquake cycle in the northern Chile subduction zone.
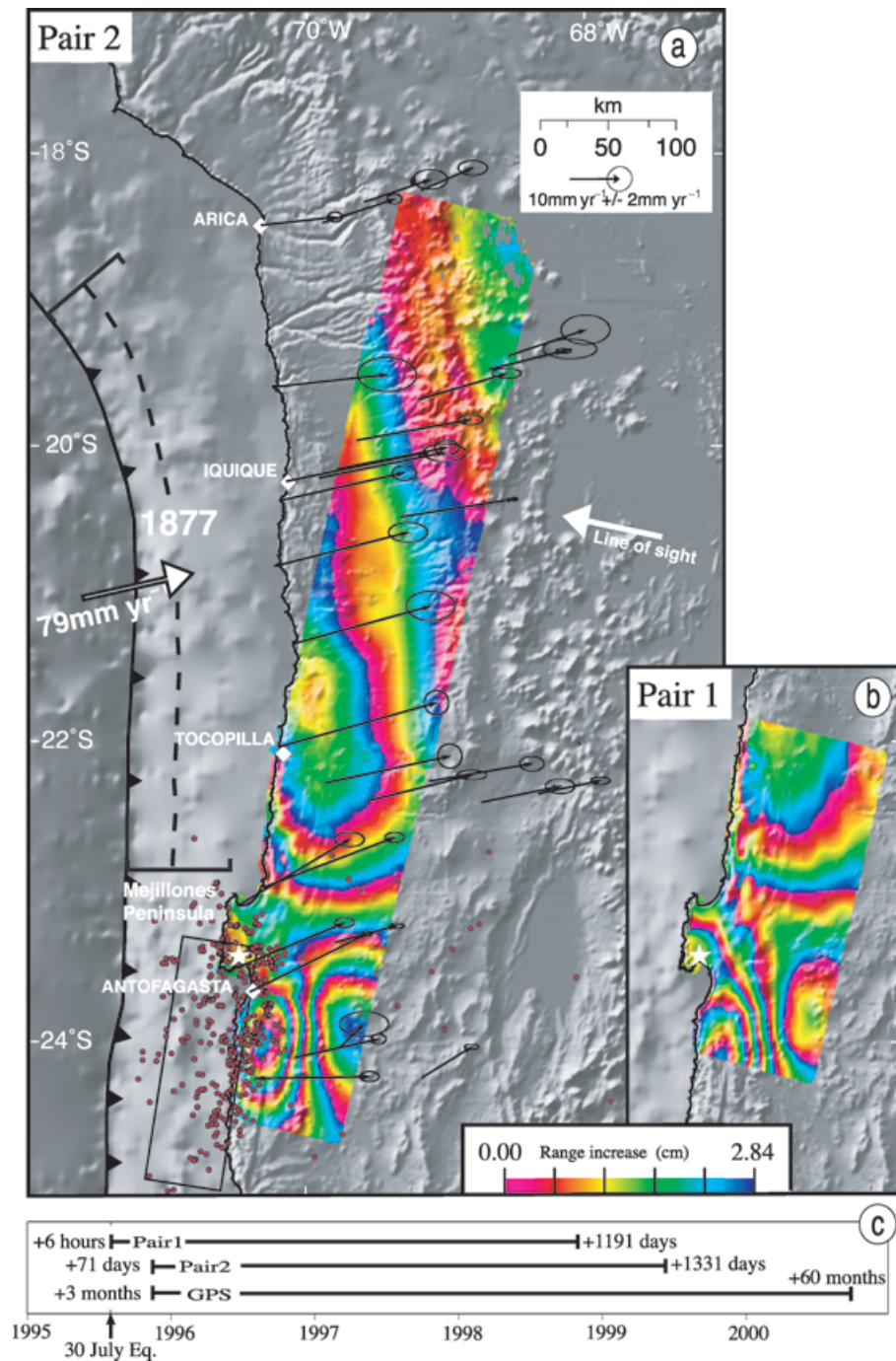
Figure 3. Post-earthquake interferograms (a, b) and date of observation (c). These interferograms were calculated using two ERS radar passes separated respectively by (a) 3.6 yr and (b) 3.3 yr. We used descending satellite track 96. Details of the orbits are given in Table 1. The two interferograms are represented in the radar line of sight direction (white arrow, westward) from the satellite to the ground direction projected onto the ground. A complete colour cycle (pink, yellow, green, blue) corresponds to a 2.84 cm increase in distance (range increase) between the radar and the Earth's surface. (a) Interferogram beginning 71 days after the Antofagasta earthquake. The area mapped is about 700 km long by 100 km wide (seven radar images). The 1995 Antofagasta rupture is marked by the rectangle, with the epicentre (white star) and aftershocks (red dots). The approximate segment that ruptured in 1877 is shown by the dashed line parallel to the trench. The GPS vectors (black arrows) are represented relative to stable South America as the plate convergence vector (white arrows, seawards) from the Nuvel-1A model (DeMets *et al.* 1994). (b) The first image used to calculate this interferogram was taken 6 hr after the earthquake. It is composed of two and a half frames totalling about 250 × 100 km². Topography and bathymetry (background) are extracted respectively from GTOPO30 and the bathymetry grid has a 3′ resolution. (c) Date of observation of each interferogram and the GPS campaign after the 1995 July 30 Antofagasta earthquake.
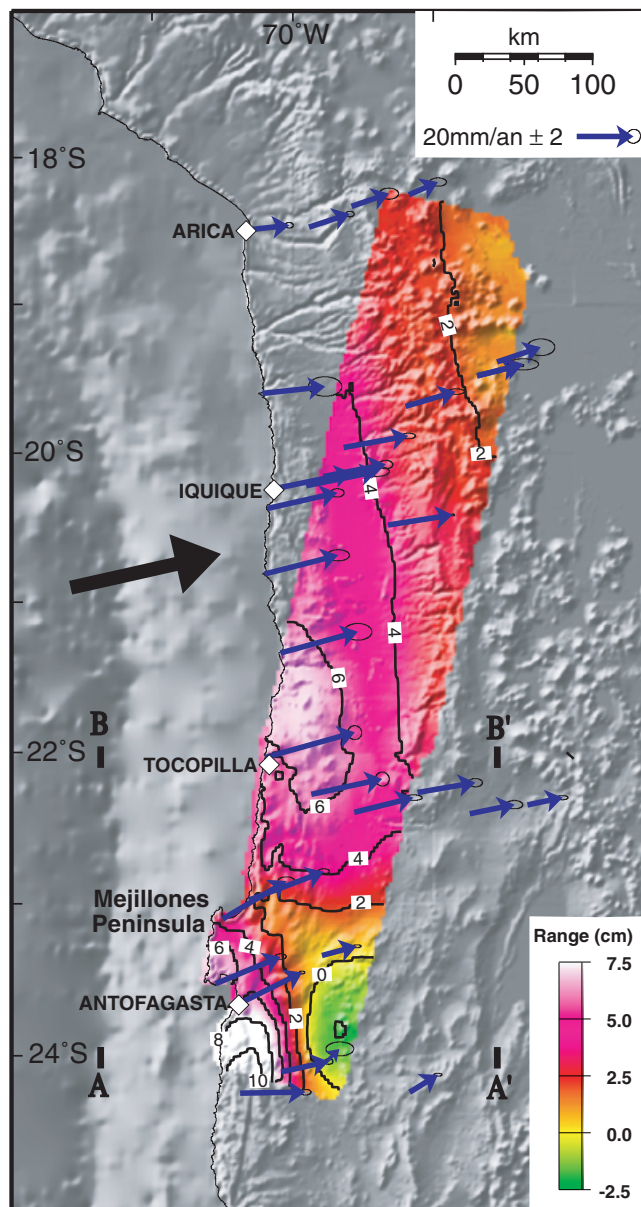
Figure 4. Unwrapped composite interferogram and GPS measurements. The interferogram is composed of Pair 1 in the southern part for the most complete post-seismic deformation (+6 hr to 1191 days after the main shock; Fig. 3b) and Pair 2 for the widest coverage of the interseismic deformation in the northern part (Fig. 3a). The colour scale refers to change in the radar line of sight direction (see Fig. 3a) with contour lines every 2 cm. The GPS velocity field (blue arrows) is relative to stable South America from GPS campaigns 1996–2000 (see Appendix, Table A1). The error ellipses are inscaled 95 per cent confidence ellipses.

3.2.1 GPS campaigns

The GPS measurements in the North Chile area began in 1991 with the installation of a 17-site transect of about 150 km length, between the Pacific coast near Iquique (20°N) and the Chilean Altiplano. This first network was completed in 1992 by the installation of three other transects: seven points at the latitude (18°S) of Arica, seven points at the latitude (22°S) of Tocopilla, nine points in the Antofagasta area (24°S) and eight additional sites in the coastal zone between Arica and Antofagasta. These 48 sites cover the entire zone corresponding to the current seismic gaps known in northern

Chile. The main disadvantage of this early GPS network is that the measurements were carried out with the first-generation GPS instruments (Ashtech L-12 and P-12 GPS receivers). Moreover, our 1991 and 1992 GPS campaigns occurred before the establishment of the International GPS Service (IGS) global network; thus there was no way to tie our network to a global reference frame (ITRF), when no permanent fiducial station (except SANT, Santiago) was available in South America.

The southern part of this network, near Antofagasta, was remeasured using the same instruments in 1995 August, soon after the occurrence of the $M_w = 8.1$ Antofagasta earthquake. The data set combining GPS 1992 and 1995 observations was used to estimate the coseismic deformation associated with this large earthquake (Table 2, Fig. 2) and helped the modelling of the source mechanism (Ruegg *et al.* 1996; Ihmlé & Ruegg 1997). The network was completely remeasured in 1996 using nine Ashtech Z12 receivers, all sampling every 30 s. The antennas used were Ashtech type I and II. Each site was surveyed for 20–30 hr on average for 2 or 3 days of independent measurement. The network was again measured in 2000, using Ashtech Z12 receivers and choke-ring antennas, during sessions lasting about 48–100 hr.

3.2.2 Permanent GPS stations

In the beginning of 1995 we initiated continuous GPS measurements at two sites at the centre of the investigated region (UAP0, located at the Arturo Prat University of Iquique, and POZ0, located 37 km east inland). The data were sampled every 30 s using Z-12 receivers and choke-ring antennas. This first installation operated for 3 months through to 1995 March. In 1995 August the receivers were reinstalled more permanently and operated quasi-continuously. The POZ0 station operated until the end of 1996 and then moved to another site PIC0 (in Pica, 90 km inland), where GPS data were collected up to the present but with some long interruptions due to power failures or maintenance problems. Nevertheless, these two permanent stations provide a long time span of GPS data to determine the interseismic loading rate of the region, and for monitoring its seismic cycle. The use of our two continuous GPS stations in the Iquique region permitted us to have time-series (see Figs A1–A3 in the Appendix) long enough to provide reliable velocity estimates in northern Chile referred to the relatively undeforming part of the South American continent.

3.2.3 Analysis

The analysis of the GPS data follows the now standard procedures described by (Feigl *et al.* 1993) and (McClusky *et al.* 2000) using the software packages GAMIT (King & Bock 1998) and GLOBK (Herring 1998). We calculated daily solutions in which we estimated station coordinates, satellite state vectors, seven tropospheric zenith delay parameters and phase ambiguities using double-difference phase measurements. We applied azimuth- and elevation-dependent antenna phase centre models. Seven IGS stations operating in neighbouring parts of South America (AREQ, BRAZ, EISL, FORT, LPGS, OHIG, SANT) were included in the processing to serve as ties with the International Terrestrial Reference Frame ITRF97 (Boucher *et al.* 1999). We used the IGS final orbits and IERS Earth rotation parameters, and applied IGS tables for azimuth and elevation corrections of the antenna phase centre.

3.2.4 Velocity solution

In a second step, the least-squares adjustment vectors and their corresponding variance–covariance matrix for station positions and

Table 2. Summary of the displacements (D$_E$ and D$_N$, the east and north components, respectively) associated with the 1995 July 30 Antofagasta earthquake ($M_w = 8.1$) estimates from GLOBK version 5.04. σ_E and σ_N correspond to formal 1σ uncertainties (for the east and north components, respectively, in mm) and Corr. relates to the correlation coefficient between the two components.

SITE	Long. (deg)	Lat. (deg)	D$_E$ (mm)	D$_N$ (mm)	σ_E error	σ_N error	Corr.
DO6	−69.166	−24.236	−241.5	14.5	8.5	5.2	0.030
DO5	−69.769	−24.045	−504.0	−7.0	17.0	10.0	0.030
BAQ	−69.781	−23.342	−260.0	−99.8	7.7	4.3	0.047
DO4	−70.080	−24.105	−825.1	−8.3	9.1	6.4	0.050
DO3	−70.308	−24.127	−950.0	−100.0	18.0	11.0	0.060
DO2	−70.373	−24.244	−878.0	−119.0	9.3	5.7	0.061
AN0	−70.405	−23.669	−784.0	−265.0	9.4	5.5	0.075
DO1	−70.440	−24.260	−828.0	−156.0	46.0	21.2	0.317
JLP	−70.546	−23.526	−481.0	−37.1	9.4	5.2	0.089

other parameters, obtained for each daily GAMIT solution, were combined using the GLOBK software (Herring 1998) to estimate the station positions and velocities in the ITRF reference frame. We first defined the reference frame by constraining the positions and velocities of four IGS stations in stable South America (KOUR, FORT, BRAZ and LPGS) to their known ITRF97 values (Boucher *et al.* 1999). In our GLOBK adjustment, the fiducial stations are constrained to 1 cm for north and east coordinates, and to 3 cm for elevation; 1 mm yr^{-1} for north and east velocities and 10 mm yr^{-1} for vertical velocity. The other stations are less constrained to 5 m in position and 25 cm yr^{-1} in velocity. The velocities obtained in ITRF97 are shown in the left part of Table A1 in the Appendix. The site velocities are calculated with respect to the stable part of South America by subtracting from our ITRF estimation the motion predicted at each station by the Nuvel-1A no-net-rotation model (Argus & Gordon 1991; DeMets *et al.* 1994). In Table A1 we also display the resulting estimated velocities with respect to the stable part of the South American Plate.

Figs 3 and 4 map the GPS velocity field in the stable South America reference frame. The observed velocity decreases strongly from the coast of Chile to the interior of South America (here limited to the Chile–Bolivia border). The coastal points show relative velocities in the range of 12–30 mm yr^{-1}, whereas the points located at the Altiplano move more slowly, at 10–20 mm yr^{-1}.

The average direction of all velocity vectors (relative to the South American (SOAM) craton) falls in the range of 75° N ± 8°, within a few degrees of the relative plate convergence (Fig. 1). The relative plate velocity between the Nazca and SOAM plates is in the range of 79–83 mm yr^{-1} (respectively at 20°S and 38°S), with a mean convergence direction of about 77°N, according to estimations along the Chilean coast from current plate motion models (Argus & Gordon 1991).

4 MODELLING

4.1 Modelling approach

The geometry of the interplate interface for the Antofagasta rupture segment and the area north of it, reaching the Arica corner, has been presented by Comte & Suárez (1995), based on local seismic observations, and constitutes an excellent basis for our modelling of the Antofagasta source and post-seismic processes. We also used the aftershocks following the 1995 Antofagasta earthquake, relocated with a local network (Delouis *et al.* 1997), to position the thrust interface in the Antofagasta area. The geometry adopted is constant along strike, but includes a gradual change of dip from 10° at the trench to 30° below 100 km depth (see Fig. 7c). The kinematic boundary conditions are fixed to the convergence rate of 79 mm yr^{-1}

with respect to South America from the Nuvel-1A model (Argus & Gordon 1991; DeMets *et al.* 1994). This assumption also sets the rake to be consistent with the observation of no slip partitioning as proposed by previous studies (Ruegg *et al.* 1996; Klotz *et al.* 1999). Our solutions allow for small amounts of backarc shortening in the sub-Andean region, again consistent with previous observations (Bevis *et al.* 2001; Klotz *et al.* 2001).

The Peru–Chile subduction zone is characterized by a curved geometry along strike, with a 55° bend at Arica and along-dip curvature, which is not easy to model using rectangular dislocations. In order to include complexities associated with the curvature of the subduction zone, we adopt a code based on Okada's formulation (Okada 1985) for dislocations in an elastic half-space, with point sources simulating slip over small patches of the fault. The slab interface is meshed into small triangular elements with a point source located at each element centroid.

Although time-dependent post-seismic relaxation associated with viscous flow following thrust events has been proposed as a possible mechanism to explain the relaxation (Thatcher & Rundle 1984; Cohen 1999), here we will focus exclusively on elastic processes. Our modelling approach is divided into two steps. First, we look for the interseismic model that best fits the geodetic observations from the Arica corner to the North Mejillones Peninsula. We apply this model uniformly along the trench, and we invert the residual deformation field in the Antofagasta area in a second step, thus modelling the post-seismic relaxation as afterslip. The final model is the sum of these two intermediate models.

4.2 Modelling the interseismic period

We use a forward elastic slip model to fit both GPS and InSAR data observed north of the Mejillones Peninsula. This model is uniform and imposed along the Peru–Chile trench, including the region affected by the 1995 earthquake. The depth location and width of the segment locked between the earthquakes are critical parameters for seismic risk analysis. Here, we estimate the downdip extent of the northern Chile seismogenic zone. The updip limit of the locked zone is taken to be at the trench, at a depth of 7 km, though perhaps it would be more correct to place it at a depth of 20 km, as reliably determined further to the south by Husen *et al.* (1999), from Antofagasta 1995 aftershocks. Still, the models tested are mostly sensitive to the down-dip limits of the locked and transition zones.

The simplest model for the subduction thrust earthquake cycle considers an edge dislocation in elastic half-space. In so-called 'back-slip' models, the zone locked during the interseismic phase is modelled with dislocations in the opposite sense to the coseismic slip (Savage 1983). Here, taking into account the seismicity, we define a curved slab geometry, and we do not use the back-slip

model because it leads to a biased inference about the geometry of the locked portion of the thrust fault (Vergne *et al.* 2001). We prefer a forward-slip model with the deeper part slipping stably, at the plate velocity, imagining that beyond the down-dip extension of the locked zone faults move by continuous stable sliding or plastic creep. The reason for not using the back-slip is that the steady-state term modelled does not take into account the dip-angle variation of the thrust interface at depth which leads to deformation that cannot be neglected.

The maximum of interseismic deformation observed by InSAR, in a cross section at latitude 22°S (Fig. 5a), constrains the widths

of the locked zone and transition zones. We tested many models without a transition zone. These models, with the down-dip limit of the locked seismogenic zone ranging from depths of 40 to 50 km, explain the GPS observations but not the InSAR data (Fig. 5a). The peak of InSAR data is reproduced for a model locked at a depth of 45 km, without a transition zone, but the modelled peak is narrower than the observed one.

A better approximation than strictly locked and unlocked portions of the fault includes a transition zone at the down-dip extension of the seismogenic interface. An abrupt termination represents a strain singularity and is physically unrealistic. To describe a change from fully stick-slip to fully steady plastic motion, we adopt a model with a transition zone. Figs 6 and 7 show detailed map views and sections across this model. The slip rate in the transition zone
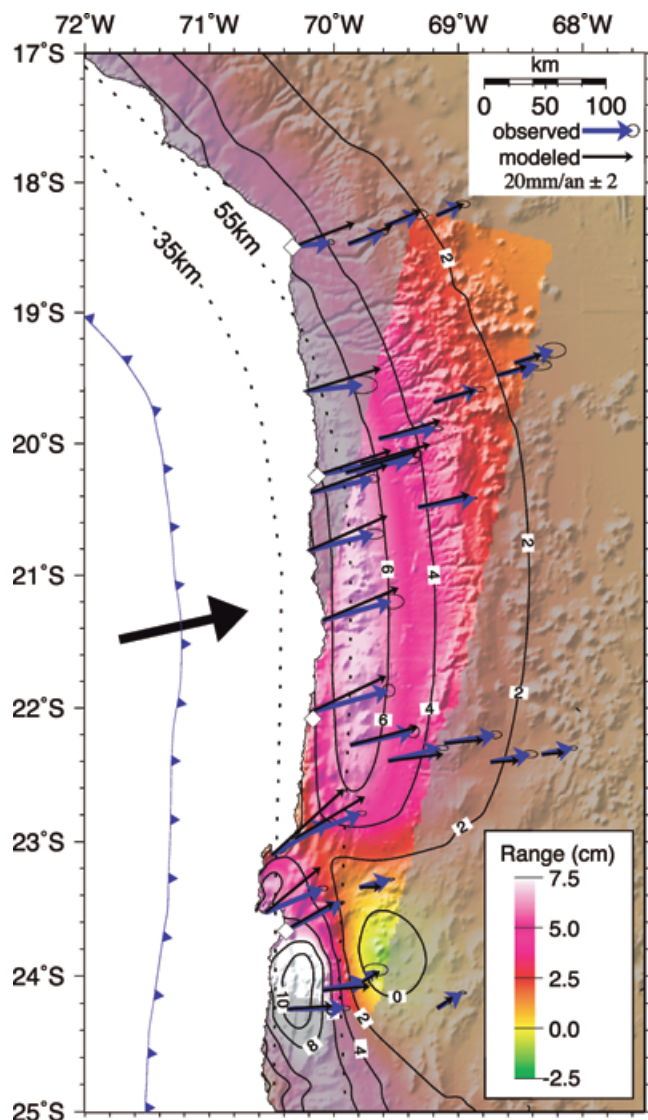

Figure 5. Profiles A–A′ and B–B′ shown in Fig. 2 and Fig. 4 of topography and geodetic data at respective latitudes (a) 22°S and (b) 24°S. (a) Top: topography. Middle: observed interseismic InSAR data (heavy line) and elastic models without a transition zone, fully locked from the surface up to a depth of 40 km (dashed line), up to a depth of 50 km (dotted line) and the model fully locked up to a depth of 35 km with a transition zone between a depth of 35 and 55 km. Bottom: same models compared to horizontal velocities of the GPS points projected in the direction N90°E, perpendicular to the average trench direction. (b) InSAR data of the coseismic deformation (CO-) and of that 3.3 yr after the earthquake (POST-).

Figure 6. Elastic model of the interferogram and GPS data presented in Fig. 4. Solid curves with labels (in cm) represent the modelled range change and the coloured stripe of the InSAR data. The fit of the modelled velocities to the GPS data is good, but stations along the coast show a systematic misfit due to the simple geometry of our model. Introducing a slightly shallower subduction interface under those stations resolves this discrepancy without modifying the main arguments in this paper. Dotted lines at depths of 35 and 55 km mark depth contours of the upper surface of the subducted Nazca Plate.

increases linearly with depth, from zero to the full plate rate, while the shallow seismogenic zone remains fully locked during the interseismic interval.

4.3 Modelling the post-seismic period

We inverted the residual obtained by subtracting the modelled interseismic deformation from the geodetic observations. We use the same thrust interface as previously defined. The lateral extent of slip is controlled by the extent of the signal in the interferograms (Fig. 3), particularly the InSAR gradient observed on both sides of the Mejillones Peninsula. The signal could not be modelled without widespread slip over a 200 km long stretch of the subduction zone, encompassing the 1995 rupture and the Mejillones Peninsula. The depth extent of the maximum post-seismic slip rate is controlled by the location of the extrema of the post-seismic signal observed in a cross-section at 24°S (Fig. 5b). It is important to recall that other models including shallow slip are also able to explain the InSAR data but are not consistent with the orientation of our GPS vectors. Adding shallow slip changed the orientation of coastal GPS velocities towards the trench, which is not seen in either the rapid post-seismic data in Antofagasta (Melbourne *et al.* 2002) or in that from the years that follow the earthquake (see fig. 4 in Khazaradze & Klotz 2003).

Fig. 6 shows the sum of the two intermediate models. It corresponds to our best post-seismic model consistent with both the GPS and InSAR measurements. The thrust interface is characterized by two different slip behaviours. The first is consistent with an interseismic loading process north of the Mejillones Peninsula. The second represents the cumulative slip relaxation plus possible interseismic reloading that followed the Antofagasta earthquake south of the Mejillones Peninsula.

5 RESULTS AND DISCUSSION

5.1 Interseismic deformation

Fig. 7(a) shows the slip rate distribution used to produce the elastic model of Fig. 6. North of the Mejillones Peninsula, the interseismic slip rate is modelled as uniform along strike, and divided into three zones along the dip. From the surface to 35 km depth the thrust interface is fully locked. The transition zone (TZ) is between 35 and 55 km deep; below it the thrust interface moves at the plate convergence rate. South of the Mejillones Peninsula the distribution of slip rate along the plate interface is heterogeneous, with an area underneath and south of the Mejillones Peninsula moving faster than the plate velocity. This is the area that experienced the 1995 Antofagasta earthquake.
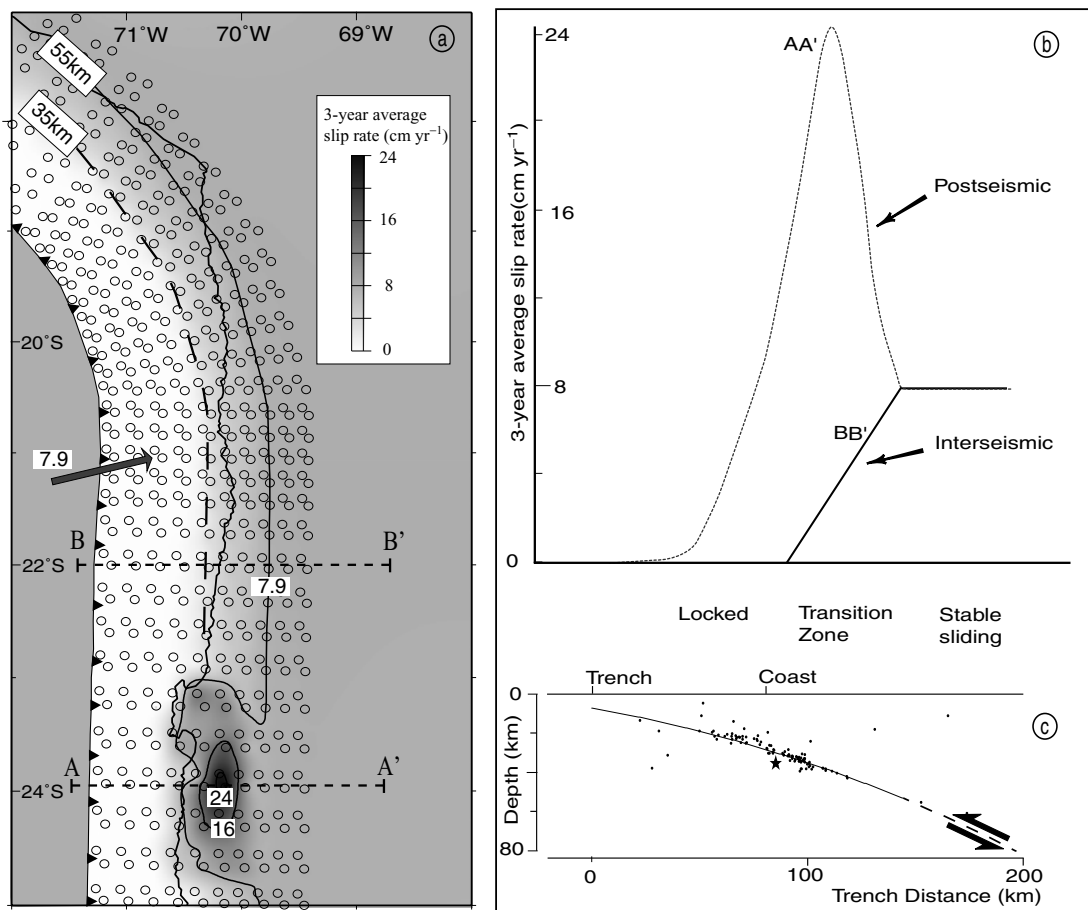

Figure 7. Modelled average slip rate on the subduction thrust interface. (a) Average slip rate distribution applied to produce Fig. 6 in an elastic half-space. Circles show the distribution of source point used to determine the thrust interface. In the north, the model is composed of a stick-slip (locked) zone to 35 km depth, a stable sliding zone with 7.9 cm yr⁻¹ of slip below 55 km, and in between a linearly increasing slip in a transition zone (profile B–B′). (b) In the area affected by the 1995 Antofagasta earthquake, a large zone of accelerating slip located in the down-dip extension of Antofagasta rupture reaches a maximum of 24 cm yr⁻¹ in the A–A′ profile. B–B′ represents the interseismic profile at 22°S. (c) A–A′ cross-section of the subduction interface with aftershocks (dots) and the epicentre (star) of the Antofagasta earthquake.

In cross-section Fig. 7b shows the 3.3 yr average slip rate obtained along the A–A′ (24°S) and B–B′ (22°S) profiles. The A–A′ transect is in the area affected by the relaxation process, and B–B′ in a region of pure interseismic loading (Fig. 7a). The maximum relaxation slip rate along the A–A′ transect is located at the centre of the transition zone and reaches three times the rate of plate motion. Assuming that the interseismic loading observed in the north also occurred in the Antofagasta area after the earthquake, we estimate the post-seismic relaxation slip as the difference between the observed relaxation rate A–A′ and the purely interseismic rate B–B′. In the lower part of the transition zone, the slip rate of relaxation process A–A′ has a negative slope while the interseismic loading B–B′ has a positive one. This is consistent with the result seen in theoretical models (Tse & Rice 1986), adapted to the subduction context by Stuart (1988) and Kato & Hirasawa (1997), in which seismic rupture in the shallow, velocity-weakening part of the rupture zone transfers large stresses to the inherently stable velocity-strengthening zone down-dip, causing that zone to slide transiently at much higher rates to relax those stresses.

During the last decade there have been many GPS campaigns in the Central Andes. An integrated crustal velocity field was proposed by Kendrick *et al.* (2001) including both the South America–Nazca Plate Project (SNAPP) (Norabuena *et al.* 1998), based in Bolivia and Peru, and the Central Andes GPS Project (CAP) (Bevis *et al.* 1999), based in northern Chile and Argentina. A velocity bias was observed between our GPS velocity and that first published by Norabuena *et al.* (1998). The correction proposed by Kendrick *et al.* (2001) is more consistent with our observations. Our common GPS velocity points presented here agree well with those of CAP in both amplitude and direction. Bevis *et al.* (2001) decomposed the GPS velocity field into two parts: the first attributed to a fully locked zone at depths of 10–50 km, the second to a smaller absorption of the back arc shortening estimated at 9.5 mm yr^{-1} near 18.5°S and as about 6.5 mm yr^{-1} near 21.5°S. Because our measurements are limited in the Chilean forearc region, it is difficult for us to estimate the fraction of motion transferred to the sub-Andean underthrusting. Nevertheless an average value of 6 mm yr^{-1} from 18°S to 25°S falls within the uncertainties of our GPS model (Fig. 6).

Models based solely on the available GPS measurements are insensitive to the width of the transition zone, but coupled studies using both GPS and InSAR provide a more detailed description of the deeper part of the seismogenic zone. The maximum depth of the seismogenic zone proposed here is 55 km divided into a fully coupled zone up to a depth of 35 km and a linearly decreasing coupling zone below. By comparison with seismological observations, our conclusions are in the range of 36–41 km depth as proposed by Tichelaar & Ruff (1993) based on the presence of thrust interplate events of magnitude 6 or larger and of 60 ± 10 km as proposed by Comte & Suárez (1995) using teleseismically recorded earthquakes.

Studies based on thermal data argue that temperature controls the down-dip limit of seismogenic behaviour along the subduction thrust. The landward end of the locked zone may occur at the transition from brittle to ductile or velocity-weakening to velocity-strengthening beginning at 350 °C for common continental crustal rocks (Hyndman & Wang 1993). These authors postulate a transition zone from the fully stick-slip regime near 350 °C to fully steady-slip over 450 °C. When the 350 °C isotherm is as deep as it is in the northern Chile subduction zone, the intersection of the interface thrust with the continental forearc Moho can also explain the down-dip limits of the seismogenic area (Oleskevich *et al.* 1999). Recent observations using *P-S* wave conversion suggest an inter-

section with the Moho at a depth of 40 to 50 km, deepening to the east (The ANCOR Working group 1999; Bock *et al.* 2000). Patzwahl *et al.* (1999) show a portion of the Moho dipping eastwards from 43–50 km near the coast to 55–64 km up to about 240 km inland from wide-angle seismic measurements. This means that the interplate interface meets the Moho at depths of 43–50 km, which is the depth range of the transition zone in the area of our study.

5.2 Post-seismic deformation

In the post-seismic interferogram, the area that underwent coseismic subsidence is both rising and subsiding (compare the map views in Figs 2 and 4). A cross-section through that area, along 24°S, shows that the minimum of the post-seismic signal is farther from the trench than the coseismic minimum, suggesting that a deeper process occurred during the post-seismic relaxation (Fig. 5b). A comparison between the coseismic and the 3.3 yr post-seismic slip distribution (Fig. 8) indicates that post-seismic relaxation affected an area as wide as the coseismic slip distribution. Modelled coseismic slip reaches approximately 5.5 m at a depth of 30 km (Fig. 8a). The post-seismic slip release (Fig. 8b) is deeper than the coseismic slip, reaching 80 cm of slip at a depth of 45 km in the 3.3 yr that followed the 1995 July earthquake. There is also post-seismic slip that spreads laterally along strike, over around 30 km toward the north, underneath the Mejillones Peninsula.

InSAR and GPS measurements in the 3.3 yr following the 1995 main shock also include coseismic slip from the series of ($M_w \geq 6.0$) earthquakes that occurred on or close to the interplate interface during that time. The epicentres and mechanisms of these earthquakes are presented in Fig. 8(b). It is plausible that the occurrence of all these events is a result of stress redistribution in that area caused by the source processes of the 1995 Antofagasta earthquake. The first three of these earthquakes had the magnitudes $M_w \sim 6.0$–6.4 and were early shallow aftershocks (around 25 km deep). Because of their magnitudes they probably added a little (locally, of the order of 10 cm) to the post-seismic slip. The two largest, deeper events of $M_w = 6.6$ at a depth of 49 km in 1996 April and $M_w = 7.1$ at a depth of 42 km in 1998 January (Fig. 8b, epicentres from the USGS catalogue) must have contributed appreciable slip. However, the amount and extent along strike of the slip associated with these events appear smaller than those we infer from the interferometric signal. The contribution of these events can be removed from the cumulative post-earthquake slip to yield the aseismic slip (Fig. 8c). The moment release of all of the seismic events in the 3.3 yr that followed the Antofagasta earthquake of 1995 July is approximately 6×10^{19} N m. The modelled post-seismic moment release as shown in Fig. 8(b) is 1.55×10^{20} N m. The comparison suggests that around 60 per cent of the signal (1×10^{20} N m) corresponds to aseismic slip in this time period (Fig. 8c). Uniform down-dip slip appears to encompass the segment that ruptured during the 1995 earthquake. Lateral slip with a peak at a depth of 30 km beneath the Mejillones Peninsula is needed to fit both GPS and InSAR data. This lateral slip is consistent with the time behaviour of the aftershock activity (Delouis *et al.* 1997) and the low *b* value observed below the peninsula (Sobiesiak 2000). The 1995 Antofagasta earthquake and the post-seismic slip that followed clearly increased the stress underneath Mejillones Peninsula, loading the 1877 seismic gap from the south.

The eastward orientation of GPS vectors indicates that interseismic loading dominated the horizontal deformation field between 1996 October and 2000 October in the Antofagasta area. Recent
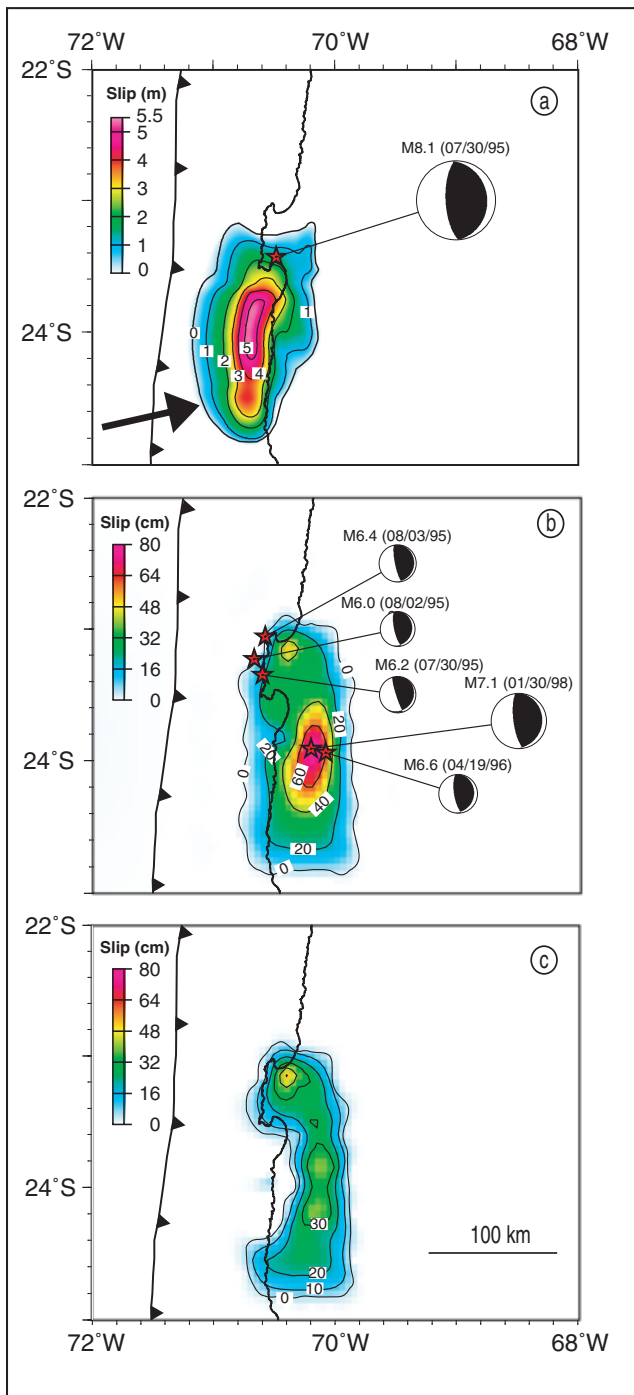
GPS velocities (Khazaradze & Klotz 2003), showing the temporal variations of GPS velocities in the years 1995–1996 and 1996–1997, and located at the coast as well as further inland suggested that a disorganized deformation field motion occurred in that area. That study suggested that interseismic effects begin to dominate the post-seismic effects after 1 yr. Taking into account interseismic loading, as estimated along the northern adjacent segment, we find 80 cm of post-earthquake cumulative slip. That number would diminish to around 60 cm if the interseismic loading were not accounted for.

It has been proposed by Melbourne *et al.* (2002) that there was no post-seismic deformation in the Antofagasta area following the 1995 July earthquake, based on the observation of the continuous GPS station in the coastal city of Antofagasta. The two horizontal components of GPS (fig. 5 in Melbourne *et al.* 2002) suggest that no post-seismic deformation appears. It is not surprising that the authors do not detect any horizontal displacement as evidence of moment release in Antofagasta city, which is mainly influenced by the interseismic reloading that followed the $M_\mathrm{w} = 8.1$ earthquake. The coastal city of Antofagasta is too far from the area affected by the post-seismic slip, but GPS stations located roughly 100 km from the coast (Fig. 2 in this study and fig. 4 in Khazaradze & Klotz 2003) clearly show a change both in the northern component and in amplitude in the 3–4 yr that followed the earthquake. This shows the importance of the continuous GPS station location for recording some post-seismic deformation and explains why Melbourne *et al.* (2002) did not detect post-seismic signal. Also, for the $M_\mathrm{w} = 8.4$ South Peru earthquake of 2001 June, the permanent GPS tracking station at Arequipa, roughly 100 km from the coast, shows several centimetres of post-seismic release (Ruegg *et al.* 2001; Melbourne *et al.* 2002).

5.3 Composition of an earthquake cycle in the Antofagasta area

The temporal behaviour of slip along the interplate interface during the earthquake cycle is composed of the following three parts:

(1) During the interseismic period, while the main seismogenic zone remains locked, the deeper part moves stably with the slip rate increasing from zero to the plate velocity in the transition zone.

(2) The earthquake coseismic slip ruptures the main seismogenic zone and part of the transition zone.

(3) Post-seismically, the transition zone accelerates to recover the long-term average slip rate on the thrust interface.

An earthquake cycle model consistent with deformation observed in Antofagasta and surrounding regions appears in Fig. 9. We assume that the interseismic loading rate in the Antofagasta area, the same as in the segment north of it, is 79 mm yr^{-1} and constant in time. To reach the maximum coseismic slip of 5.5 m requires 70–75 yr of interseismic slip. In accord with a slower convergence rate of 64 mm yr^{-1} as proposed by the GPS data (see Angermann *et al.* 1999; Sella *et al.* 2002), at least 85 yr of interseismic slip are required. The Antofagasta earthquake initiates (star in Fig. 9c) in a strongly coupled area and coseismic slip propagates both towards the surface and into the transition zone. Co- and interseismic slip interpenetrate each other in the transition zone; their sum is not uniform along dip and a gap of slip appears in the transition zone. This gap is partially filled during the years that follow the earthquake, contributing to an adjustment towards a more uniform slip on the thrust interface throughout the earthquake cycle. The same effect appears in the theoretical models with depth-variable friction
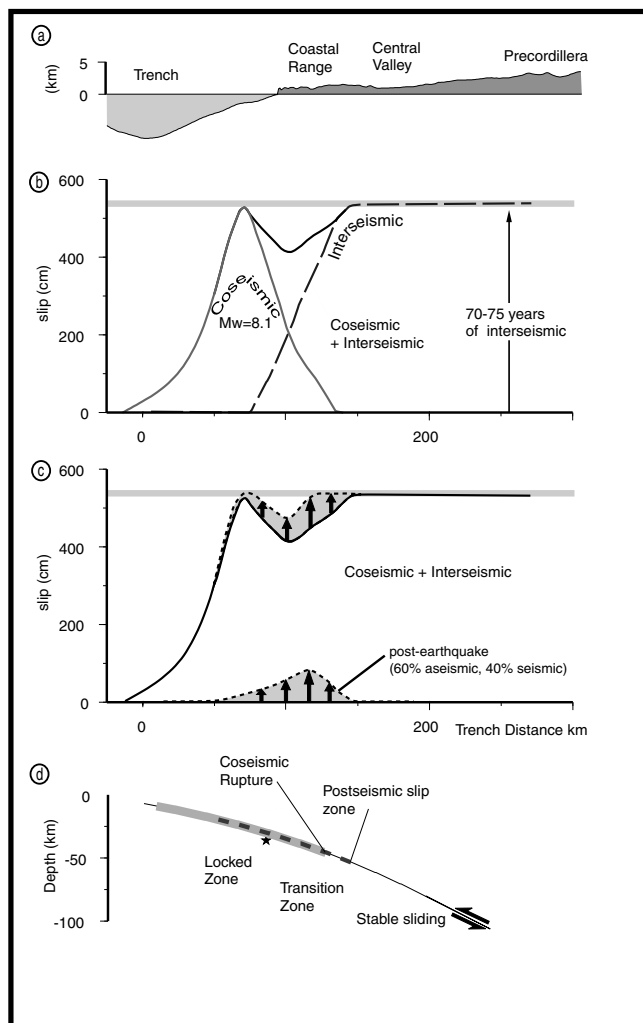

Figure 8. Comparison of (a) the coseismic, (b) the 3.3 yr cumulative post-earthquake slip distribution associated with the Antofagasta earthquake and (c) the net post-earthquake aseismic slip. (a) Map view of the coseismic slip associated with the 1995 July 30 Antofagasta earthquake. The contour interval of coseismic slip is 1 m. (b) Map view of the cumulative slip in the 3.3 yr following the 1995 July 30 Antofagasta earthquake. The contour interval is 20 cm. The CMT of earthquakes with $M_\mathrm{w} \geq 6$ in the period of observation are after Harvard and the location after USGS. (c) Map view of the aseismic afterslip after removal of slip associated with the 1996, $M_\mathrm{w} = 6.6$ and the 1998, $M_\mathrm{w} = 7.1$ earthquakes (assumed to occur on the plate interface).

Figure 9. Slip cycle model along the depth of the subduction interface. (a) Profile perpendicular to the trench and topography at latitude 24°S. (b) Coseismic slip, which reaches 5.5 m in the upper part of the thrust: 70–75 yr of cumulated interseismic slip are necessary at depth to reach a similar value. (c) The sum of coseismic and interseismic slip does not explain the whole cycle and post-seismic slip (dashed line) fills the remaining gaps with both seismic slip and aseismic shear. (d) Location of slip on the thrust interface.

(Tse & Rice 1986). These results contribute, with other geodetic studies of post-seismic deformation and transient aseismic slip (Hirose *et al.* 1999; Cohen & Freymueller 2001; Dragert *et al.* 2001; Lowry *et al.* 2001; Cakir *et al.* 2003), to shed new light on the mechanical behaviour of the lower seismogenic zone of faults, where large earthquakes commonly nucleate.

ACKNOWLEDGMENTS

REFERENCES

Angermann, D., Klotz, J. & Reigber, C., 1999. Space-geodetic estimation of the Nazca–South America Euler vector, *Earth planet. Sci. Lett.,* **171,** 329–334.

Argus, D.F. & Gordon, R.G., 1991. No-net-rotation model of current plate velocities incorporating plate motion model Nuvel-1, *Geophys. Res. Lett.,* **18**(11), 2039–2042.

Armijo, R. & Thiele, R., 1990. Active faulting in northern Chile: ramp stacking and lateral decoupling along a subduction plate boundary?, *Earth planet. Sci. Lett.,* **98,** 40–61.

Bevis, M., Smalley, R.J., Herring, T., Godoy, J. & Galban, F., 1999. Crustal motion north and south of the Arica deflection: comparing recent geodetic results from the Central Andes, *Geochem. Geophys. Geosyst.,* **1,** doi:1999GC000011.

Bevis, M., Kendrick, E., Smalley, R.J., Brooks, B., Allmendinger, R. & Isacks, B., 2001. On the strength of interplate coupling and the rate of back arc convergence in the central andes: an analysis of the interseismic velocity field, *Geochem. Geophys. Geosyst.,* **2,** doi:10.129/2001GC000198.

Bock, G., Schurr, B. & Asch, G., 2000. High-resolution image of the oceanic Moho in the subduction Nazca plate from *P-S* converted waves, *Geophys. Res. Lett.,* **27,** 3929–3932.

Boucher, C., Altamimi, Z. & Sillard, P., 1999. The 1997 International Terrestrial Reference Frame (ITRF97), *IERS Technical Note 27* Observatoire de Paris, Paris.

Cakir, Z., de Chabalier, J.B., Armijo, R., Meyer, B., Barka, A. & Peltzer, G., 2003. Coseismic and early postseismic slip associated with the 1999 Izmit earthquake (Turkey), from SAR interferometry and tectonic field observations, *Geophys. J. Int.,* **155,** 93–110.

Carlo, L.D., Lay, T., Ammon, C.J. & Zhang, J., 1999. Rupture process of the 1995 Antofagasta subduction earthquake, *Pageoph,* **154,** 677–709.

Cohen, S.C., 1999. Numerical models of crustal deformation in seismic zones, *Adv. Geophys.,* **41,** 134–231.

Cohen, S.C. & Freymueller, J.T., 1997. Deformation of the Kenai Peninsula, Alaska, *J. geophys. Res.,* **102**(B9), 20 479–20 487.

Cohen, S.C. & Freymueller, J.C., 2001. Crustal uplift in the southcentral Alaska subduction zone: a new analysis and interpretation of tide gauge observations, *J. geophys. Res.,* **106,** 11 259–11 270.

Comte, D. & Pardo, M., 1991. Reappraisal of great historical earthquakes in the northern Chile and southern Peru seismic gaps, *Natural Hazards,* **4,** 23–44.

Comte, D. & Suárez, G., 1995. Stress distribution and geometry of the subducting Nazca plate in northern Chile using teleseismically recorded earthquakes, *Geophys. J. Int.,* **122,** 419–440.

de Chabalier, J.B., Ruegg, J.C., Armijo, R., Delacourt, C., Fruneau, B., Massonnet, D., Campos, J. & Barrientos, S., 1997. Modelling the deformation related to the $M_w = 8.1$ subduction earthquake of northern Chile (1995) using SAR interferometry and GPS measurements, *EOS. Trans. Am. geophys. Un., Fall Meet. Suppl.,* F696.

de Chabalier, J.B., Ruegg, J.C., Armijo, R., Massonnet, D., Fruneau, B., Vadon, H., Delacourt, C. & Campos, J., 1998. Modelling the deformation related to the $Mw = 8.1$ Antofagasta earthquake of northern Chile (1995) using SAR interferometry and GPS measurements, *Abstracts EGS XXIII General Assembly, Nice, France, 20–24 April*.

Delouis, B. *et al.,* 1997. The $Mw = 8.0$ Antofagasta (Northern Chile) earthquake of 30 July 1995: a precursor to the end of the large 1877 gap, *Bull. seism. Soc. Am.,* **87,** 427–445.

DeMets, C., Gordon, R.G., Argus, D.F. & Stein, S., 1994. Effect of recent revisions to the geomagnetic reversal time scale on estimates of current plate motions, *Geophys. Res. Lett.,* **21,** 2191–2194.

Dragert, H., Hyndman, R.D., Rogers, G.C. & Wang, K., 1994. Current deformation and the width of the seismogenic zone of the northern Cascadia subduction thrust, *J. geophys. Res.,* **99**(B1), 653–668.

Dragert, H., Wang, K. & James, S.T., 2001. A silent slip event on the deeper Cascadia subduction interface, *Science,* **292,** 1525–1528.

Engdahl, R.E., Van der Hilst, R. & Buland, R., 1998. Global teleseismic earthquake relocation with improved travel times and procedures for depth determination, *Bull. seism. Soc. Am.,* **88**(3), 722–743.

Feigl, K.L. *et al.,* 1993. Space geodetic measurement of crustal deformation in central and southern California, 1984–1992, *J. geophys. Res.,* **98,** 21 677–21 712.

Gabriel, A.K., Goldstein, R.M. & Zebker, H.A., 1989. Mapping small elevation changes over large areas: differential radar interferometry, *J. geophys. Res.,* **94,** 9183–9191.

Goldstein, R.M. & Werner, C.L., 1998. Radar interferogram filtering for geophysical applications, *Geophys. Res. Lett.,* **25**(21), 4035–4038.

Goldstein, R.M., Zebker, H.A. & Werner, C.L., 1988. Satellite radar interferometry two-dimensional phase unwrapping, *Radio Sci.,* **23,** 713–720.

Herring, T., 1998. *Documentation for GLOBK: Global Kalman Filter for VLBI and GPS Analysis Program,* version 4.1, MIT, Cambridge, MA.

Hirose, H., Hirahara, K., Kimata, F., Fujii, N. & Miyazaki, S., 1999. A slow thrust slip event following the two 1996 Hyuganada earthquakes beneath the Bungo Channel, southwest Japan, *Geophys. Res. Lett.,* **26,** 3237–3240.

Husen, S., Kissling, E., Flueh, E. & Asch, G., 1999. Accurate hypocentre determination in the seismogenic zone of the subducting Nazca plate in northern Chile using a combined on-/offshore network, *Geophys. J. Int.,* **138,** 687–701.

Hyndman, R.D. & Wang, K., 1993. Thermal constrains on the zone of major thrust earthquake failure: the Cascadia subduction zone, *J. geophys. Res.,* **98,** 2039–2060.

Ihmlé, P.F. & Ruegg, J.C., 1997. Source tomography by simulated annealing using broad-band surface waves and geodetic data: application to the $Mw = 8.1$ Chile 1995 event, *Geophys. J. Int.,* **131,** 146–158.

Kato, N. & Hirasawa, T., 1997. A numerical study on seismic coupling along subduction zones using a laboratory-derived friction law, *Phys. Earth planet. Inter.,* **102,** 51–68.

Kelleher, J.A., 1972. Rupture zones of large south America earthquakes and some predictions, *J. geophys. Res.,* **77,** 2087–2103.

Kendrick, E., Bevis, M., Smalley, R.J. & Brooks, B., 2001. An integrated crustal velocity field for the Central Andes, *Geochem. Geophys. Geosyst.,* **2,** doi:10.1029/2001GC000191.

Khazaradze, G. & Klotz, J., 2003. Short and long-term effects of GPS measured crustal deformation rates along the South-Central Andes, *J. geophys. Res.,* **108**(B6), 2289.

King, R. & Bock, Y., 1998. *Documentation for the GAMIT GPS Analysis Software,* version 9.7, MIT, Cambridge, MA.

Klotz, J. *et al.,* 1999. GPS-derived deformation of the Central Andes including the 1995 Antofagasta $M_w = 8.0$ earthquake, *Pageoph,* **154,** 709–730.

Klotz, J., Khazaradze, G., Angermann, D., Reigber, C., Perdomo, R. & Cifuentes, O., 2001. Earthquake cycle dominates contemporary crustal deformation in Central and Southern Andes, *Earth planet. Sci. Lett.,* **193,** 437–446.

Lowry, A.R., Larson, K.M., Kostoglodov, V. & Bilham, R., 2001. Transient fault slip in Guerrero, southern Mexico, *Geophys. Res. Lett.,* **28,** 3753–3756.

Massonnet, D., Rossi, M., Carmona, C., Adragna, F., Peltzer, G., Feigl, K. & Rabaute, T., 1993. The displacement field of the Landers earthquake mapped by radar interferometry, *Nature,* **364,** 138–142.

McClusky, S. *et al.,* 2000. Global Positioning System constraints on plate kinematics and dynamics in the eastern Mediterranean and Caucasus, *J. geophys. Res.,* **105**(B3), 5695–5720.

Melbourne, T.I., Webb, F.H., Stock, J.M. & Reigber, C., 2002. Rapid postseismic transients in subduction zones from continuous GPS, *J. geophys. Res.,* **107**(B10), 2241–2251.

Nishenko, S.P., 1985. Seismic potential for large and great interplate earthquakes along the Chilean and southern Peruvian margins of South America: a quantitative reappraisal, *J. geophys. Res.,* **90,** 3589–3615.

Nishenko, S.P., 1991. Circum-Pacific seismic potential: 1989–1999, *Pure appl. Geophys.,* **135,** 169–259.

Norabuena, E., Leffler-Griffin, L., Mao, A., Dixon, T., Stein, S., Sacks, I.S., Ocola, L. & Ellis, M., 1998. Space geodetic observations of Nazca–South America convergence across the Central Andes, *Science,* **279,** 358–361.

Okada, Y., 1985. Surface deformation to shear and tensile faults in a half space, *Bull. seism. Soc. Am.,* **75,** 1135–1154.

Oleskevich, D.A., Hyndman, R.D. & Wang, K., 1999. The updip and downdip limits to great subduction earthquakes: thermal and structural models of Cascadia, south Alaska, SW Japan, and Chile, *J. geophys. Res.,* **104,** 14 965–14 991.

Patzwahl, R., Mechie, J., Schulze, A. & Giese, P., 1999. Two-dimensional velocity models of the Nazca plate subduction zone between $19.5°S$ and $25°S$ from wide-angle seismic measurements during the CINCA95 project, *J. geophys. Res.,* **104,** 7293–7317.

Peltzer, G., Crampé, F., Hensley, S. & Rosen, P., 2001. Transient strain accumulation and fault interaction in the Eastern California shear zone, *Geol. Soc. Am.,* **29**(11), 975–978.

Pritchard, M.E., Simons, M., Rosen, P.A., Hensley, S. & Webb, F.H., 2002. Co-seismic slip from the 1995 July 30 $M_w = 8.1$ Antofagasta, Chile, earthquake as constrained by InSAR and GPS observations, *Geophys. J. Int.,* **150,** 362–376.

Ruegg, J.C. *et al.,* 1996. The $M_w = 8.1$ Antofagasta (North Chile) earthquake of July 30, 1995: first results from teleseismic and geodetic data, *Geophys. Res. Lett.,* **23**(9), 917–920.

Ruegg, J.-C., Oclay, M. & Lazo, D., 2001. Co, post and pre(?)-seismic displacements associated with the M_w 8kl.4 Southern Peru earthquake of 23 June 2001 from continuous GPS measurements, *Seism. Res. Lett.,* **72,** 673–678.

Savage, J.C., 1983. A dislocation model of strain accumulation and release at a subduction zone, *J. geophys. Res.,* **88,** 4984–4996.

Scharroo, R. & Visser, P., 1998. Precise orbit determination and gravity field improvement for the ERS satellites, *J. geophys. Res.,* **103,** 8113–8127.

Sella, G.F., Dixon, T.H. & Mao, A., 2002. REVEL: a model for recent plate velocities from space, *J. geophys. Res.,* **107**(B4), 2081, doi:10.1029/2000JB000033.

Sobiesiak, M.M., 2000. Fault plane structure of the Antofagasta, Chile earthquake of 1995, *Geophys. Res. Lett.,* **27,** 577–580.

Stuart, W.D., 1988. Forecast model for great earthquakes at the Nankai Trough subduction zone, *Pageoph,* **126,** 619–641.

Thatcher, W., 1984. The earthquake deformation cycle on the Nankai Trough, southwest Japan, *J. geophys. Res.,* **89,** 3087–3101.

Thatcher, W. & Rundle, J.B., 1984. A viscoelastic coupling model for the cyclic deformation due to periodically repeated earthquakes at subduction zones, *J. geophys. Res.,* **89**(B9), 7631–7640.

The ANCOR Working group, 1999. The Seismic reflection image revealing offset of Andean subduction-zone earthquake locations into oceanic mantle, *Nature,* **397,** 341–344.

Tichelaar, B.W. & Ruff, L.J., 1991. Seismic coupling along the Chilean subduction zone, *J. geophys. Res.,* **96,** 11 997–12 022.

Tichelaar, B.W. & Ruff, J.L., 1993. Seismic coupling along subduction zone, *J. geophys. Res.,* **98,** 2017–2037.

Tse, S.T. & Rice, J.R., 1986. Crustal earthquake instability in relation to the depth variation of frictional slip properties, *J. geophys. Res.,* **91,** 9452–9472.

Vergne, J., Cattin, R. & Avouac, J.P., 2001. On the use of dislocation to model interseismic strain and stress build-up at intracontinental thrust faults, *Geophys. J. Int.,* **147,** 155–162.

Wessel, P.S. & Smith W.H.F., 1998. New improved version of the Generic Mapping Tools released, *EOS, Trans. AGU,* **79,** 579.

Wiemer, S. & Wyss, M., 2002. Spatial and temporal variability of the b-value in seismogenic volumes, *Adv. Geophysics,* **45,** 259–302.

APPENDIX

Time series in the ITRF 96/97 for the three well-measured GPS stations of Iquique (UAP0), Pica (PIC0) and Antofagasta (AN00) and velocity vectors used in this study. Presented here are Figs A1–A3 and Table A1.

Figure A1. Position time-series for continuous GPS station UPA0 (University Arturo Prat in Iquique) with respect to the ITRF96/97 showing the slope and their standard deviation for the North, East and Up components. Note: in order to obtain velocities/stable SOAM, subtract the mean velocity vector for SOAM in ITRF96 or, for example, the velocity of the LGPS IGS station UPA0: $dE = 26.4 \pm 0.1$ mm yr^{-1}, $dN = 5.2 \pm 0.1$ mm yr^{-1} (relative to LGPS).

Figure A2. Position time-series for continuous GPS station PIC0 (Pica) with respect to the ITRF96/97 showing the slope and its standard deviation for the North, East and Up components.
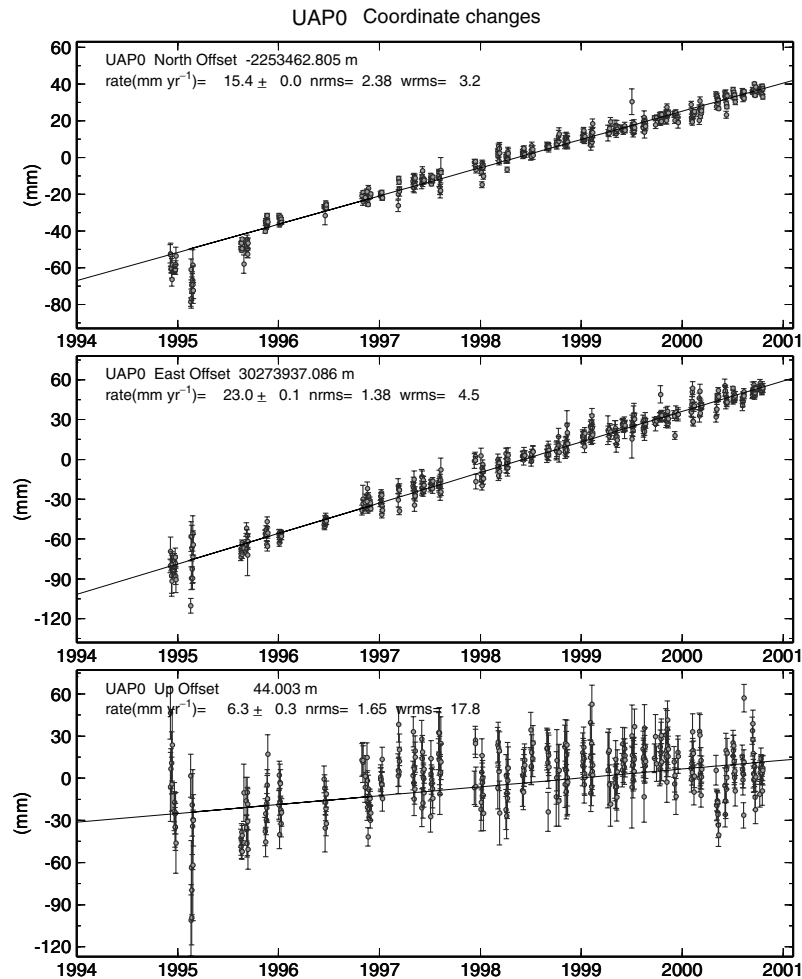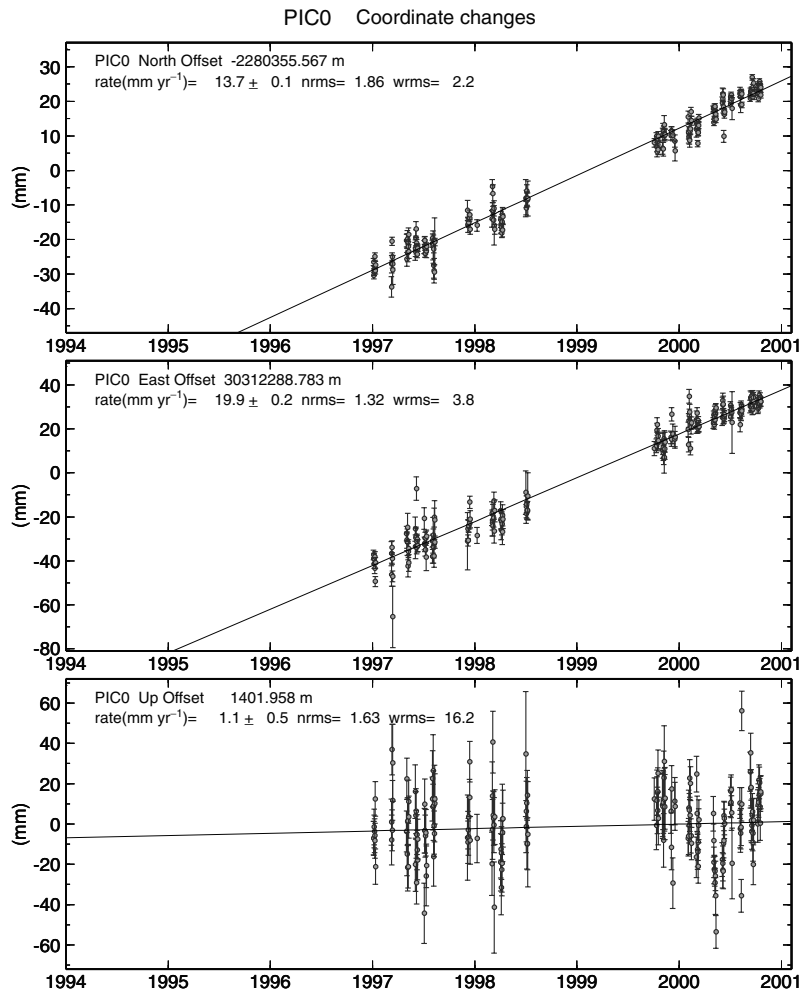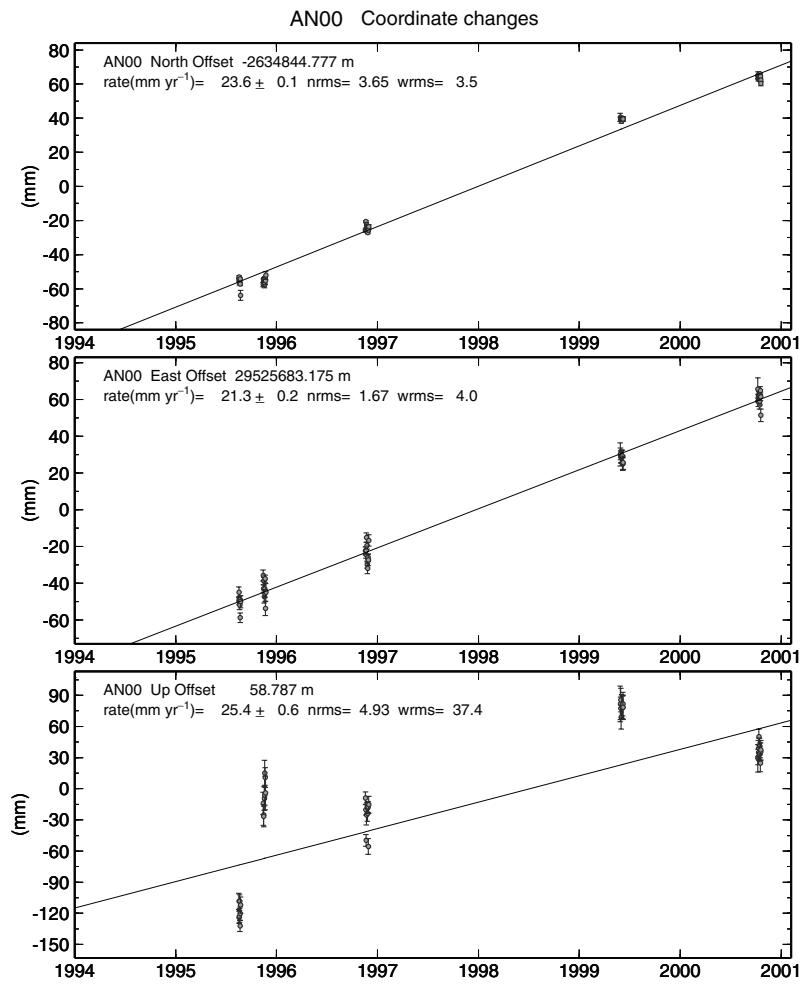
Figure A3. Position time-series for continuous GPS station AN00 (Antofagasta University) with respect to the ITRF96/97 showing the slope and its standard deviation for the North, East and Up components.

Table A1. Velocity vectors used in this study for the GPS stations in the northern Chile region, from GPS campaigns of 1996–2000. Site ID and location (in °) of GPS points (1–3). Velocities with respect to the ITRF97 (4–5) and associated formal errors (6–7) in mm yr^{-1} (1 SD). Velocities estimated with respect to South America (8–9).

Site	Lon.	Lat.	V_E	V_N	σ_E error	σ_N error	Vlon	Vlat
1	2	3	4	5	6	7	8	9
Our estimation (ITRF97)/SOAM								
FORT	−38.43	−3.877	−2.20	11.60	0.13	0.14	3.46	−0.43
KOUR	−52.81	5.252	−1.53	12.01	0.16	0.12	4.51	0.56
LPGS	−57.93	−34.907	18.20	13.70	0.18	0.14	2.44	−1.61
SANT	−76.67	−35.150	69.86	−7.02	0.76	0.51	19.11	3.96
EISL	−109.40	−27.148	0.48	9.46	0.10	0.11	69.65	−10.18
AREQ	−71.49	−16.466	11.20	12.60	0.10	0.10	14.64	2.96
UAP0	−70.14	−20.243	25.56	17.31	0.16	0.12	28.51	7.50
PIC0	−69.321	−20.485	20.60	15.20	0.25	0.13	23.56	5.29
Transect Iquique–Cariquima (Lat. 20°S)								
IQA0	−70.180	−20.373	22.40	17.10	1.00	0.60	25.32	7.30
IQD0	−69.904	−20.221	22.80	16.70	1.76	0.72	25.76	6.86
IQF0	−69.781	−20.160	19.80	15.90	1.00	0.60	22.78	6.05
IQH0	−69.636	−19.964	20.60	15.70	1.00	0.40	23.62	5.83
IQL0	−69.195	−19.686	15.50	16.80	1.20	0.40	18.58	6.88
IQN0	−68.978	−19.579	13.20	16.80	2.00	1.20	16.31	6.85
IQP0	−68.686	−19.481	12.70	15.30	0.60	0.20	15.84	5.32
IQQ0	−68.544	−19.387	14.00	15.70	2.20	0.80	17.16	5.70
CO30	−70.217	−19.598	20.00	14.00	2.40	1.40	23.04	4.20
CO50	−70.198	−20.812	23.70	18.20	1.60	0.80	26.56	8.40
CO60	−70.087	−21.340	25.10	19.10	2.00	1.20	27.88	9.29
Antofagasta area (Lat. 24°S)								
AN00	−70.405	−23.669	21.20	23.20	0.40	0.20	23.61	13.42
DO20	−70.373	−24.244	20.80	12.00	0.80	0.40	23.13	2.22
DO40	−70.080	−24.105	14.50	15.30	0.60	0.40	16.87	5.48
DO54	−69.767	−24.045	2.90	16.50	2.00	1.00	5.30	6.65
DO60	−69.166	−24.236	7.70	17.70	0.60	0.20	10.11	7.77
BAQ0	−69.791	−23.342	10.10	14.90	0.60	0.20	12.60	5.05
JLP0	−70.545	−23.526	20.60	21.10	0.80	0.40	23.02	11.34
MEJ0	−70.499	−23.102	20.30	25.00	1.20	0.60	22.79	15.24
CHA0	−70.310	−22.976	24.10	21.60	0.80	0.40	26.62	11.81
Transect Tocopilla–Calama (Lat. 22°S)								
TO10	−70.192	−22.035	29.20	20.40	1.00	1.00	31.87	10.60
TO30	−69.867	−22.279	22.80	17.00	1.00	1.00	25.46	7.16
TO40	−69.560	−22.398	18.70	16.80	1.20	0.40	21.36	6.92
TO50	−69.111	−22.267	18.20	15.10	1.00	0.60	20.91	5.17
TO60	−68.741	−22.407	13.60	14.80	1.20	0.60	16.31	4.82
TO70	−68.350	−22.349	10.20	14.20	0.80	0.30	12.95	4.18
Transect Arica–Chungara (Lat. 18°S)								
AR10	−70.322	−18.492	12.50	13.20	0.60	0.40	15.70	3.41
AR50	−69.883	−18.475	12.20	16.30	0.60	0.40	15.42	6.46
AR70	−69.522	−18.353	11.00	16.10	1.40	0.80	14.26	6.22
AR90	−69.173	−18.254	8.10	16.10	1.20	0.60	11.39	6.18